Subspace-induced Dirac point and nondissipative wave dynamics in a non-Hermitian optical lattice

Shan Li,[1] Shulin Wang,[1] Shuyue Chen,[1] Yanting Wu,[2] Shaolin Ke,[2,*] Bing Wang,[1] and Peixiang Lu[3]

[1]*School of Physics, Huazhong University of Science and Technology, Wuhan 430074, China*

[2]*Hubei Key Laboratory of Optical Information and Pattern Recognitions, Wuhan Institute of Technology, Wuhan 430205, China*

[3]*Guangdong Intelligent Robotics Institute, Dongguan 523808, China*

(Received 24 July 2021; revised 21 January 2022; accepted 25 February 2022; published 17 March 2022)

We propose a mechanism to achieve real energy spectra via Hermitian subspace in non-Hermitian systems. As an illustrative example, we investigate a system composed of two identical Su-Schrieffer-Heeger (SSH) chains connected by a lossy site in each unit cell. Although the system as a whole is non-Hermitian, it is able to support Dirac points that coexist with exceptional points, exactly exhibiting real eigenenergies. The real spectra and coexistence of different singularities are inherited from two virtual decoupled subsystems after a transformation that comprises a Hermitian SSH chain and a non-Hermitian Lieb lattice. Furthermore, we show the two subsystems both experience topological phase transition by tuning coupling strength, allowing the exploration of Hermitian and non-Hermitian topological edge modes at the same time. In aid of Hermitian subspace, the waves could evolve without dissipation depending on initial injection, which contributes to coherent splitters with locked phase and intensity in two SSH layers. The proposed model can be realized in evanescently coupled optical waveguide arrays and further extended to other tight-binding systems.

DOI: 10.1103/PhysRevA.105.033512

I. INTRODUCTION

Closed and lossless physical systems are subjected to Hermitian Hamiltonians, which guarantee realness of eigenvalue and conservation of energy. On the other hand, open systems that underlie material gain or loss or interact and exchange energy with their surrounding environment are described by non-Hermitian Hamiltonians, which commonly host complex eigenenergies with imaginary parts corresponding to growth or decay [1–10]. Their research interest is spearheaded by parity-time ($\mathcal{PT}$) symmetry, one of the most important advances in non-Hermitian physics, leading to real energy spectra in $\mathcal{PT}$-symmetric phases [11–14]. This surprising discovery develops our widespread impression that only Hermitian operators could exhibit real eigenvalues. However, $\mathcal{PT}$ symmetry is not the only constraint for real spectra. Recent studies revealed a broader class of symmetry referred to as pseudo-Hermiticity which stands for a more general condition that ensures real eigenenergies even in the presence of non-Hermiticity [15–17]. The reality of the spectra is of great significance since it guarantees the stability of physical systems despite their non-Hermitian nature. Seeking new approaches to achieve real spectra in non-Hermitian systems remains an important issue to explore.

In particular, two kinds of spectral singularities, namely, Dirac points (DPs) in Hermitian systems and exceptional points (EPs) in non-Hermitian systems, have attracted tremendous attention since they give rise to counterintuitive physics and stimulate a lot of applications. At DPs, two energy bands linearly intersect with each other in the Brillouin zone [18–21], leading to massless Dirac particles [19,22–29]. DPs behave as phase transition points of topological matters and play an important role in determining the emergence of topologically protected boundary states [30,31]. On the other hand, at EPs, eigenvalues and eigenvectors simultaneously coalesce, forming a defective eigenspace, which is in contrast to Hermitian systems with orthogonal eigenstates even at DPs [32–35]. The EPs can be differentiated by their orders, referred to as second-order EPs with two energy levels coalescing, and high-order ones with three or more levels coalescing [36–38]. A lot of remarkable phenomena are revealed at EPs or in their vicinity [9,39–44], such as chiral mode switching [45] and enhanced sensing [46]. The two kinds of singularities have a unique dispersion relation near them and thus provide versatile ways of controlling the propagation of wave packets. For example, the linear dispersion near DPs can be utilized for self-splitting without diffraction [22,25]. The flat band near EPs is useful for collimated propagation [47]. Importantly, previous works have shown that DPs and EPs are connected. By incorporating dissipation into a Hermitian system prepared with DPs, a single DP splits into a pair of EPs or is deformed into an exceptional ring [48–51].

In this work, we propose the concept of subspace, an alternative way to introduce real spectra in non-Hermitian systems, which further enables the appearance of DPs and EPs at the same time and the exploration of Hermitian and non-Hermitian topological edge modes in a single system. We design a suitable system, whose subspaces are decoupled into a Hermitian Su-Schrieffer-Heeger (SSH) model and a non-Hermitian Lieb lattice [32,52–54]. By adjusting the dissipation, two second-order EPs (EP2) coalesce into a third-order one (EP3) without affecting DPs present in the system. Moreover, we analyze the symmetry of the whole system and its subspaces and further explore the topological edge modes in this system. The bulk-edge correspondence is well figured out based on Majorana's stellar representation (MSR) [55,56].

*keshaolin@wit.edu.cn

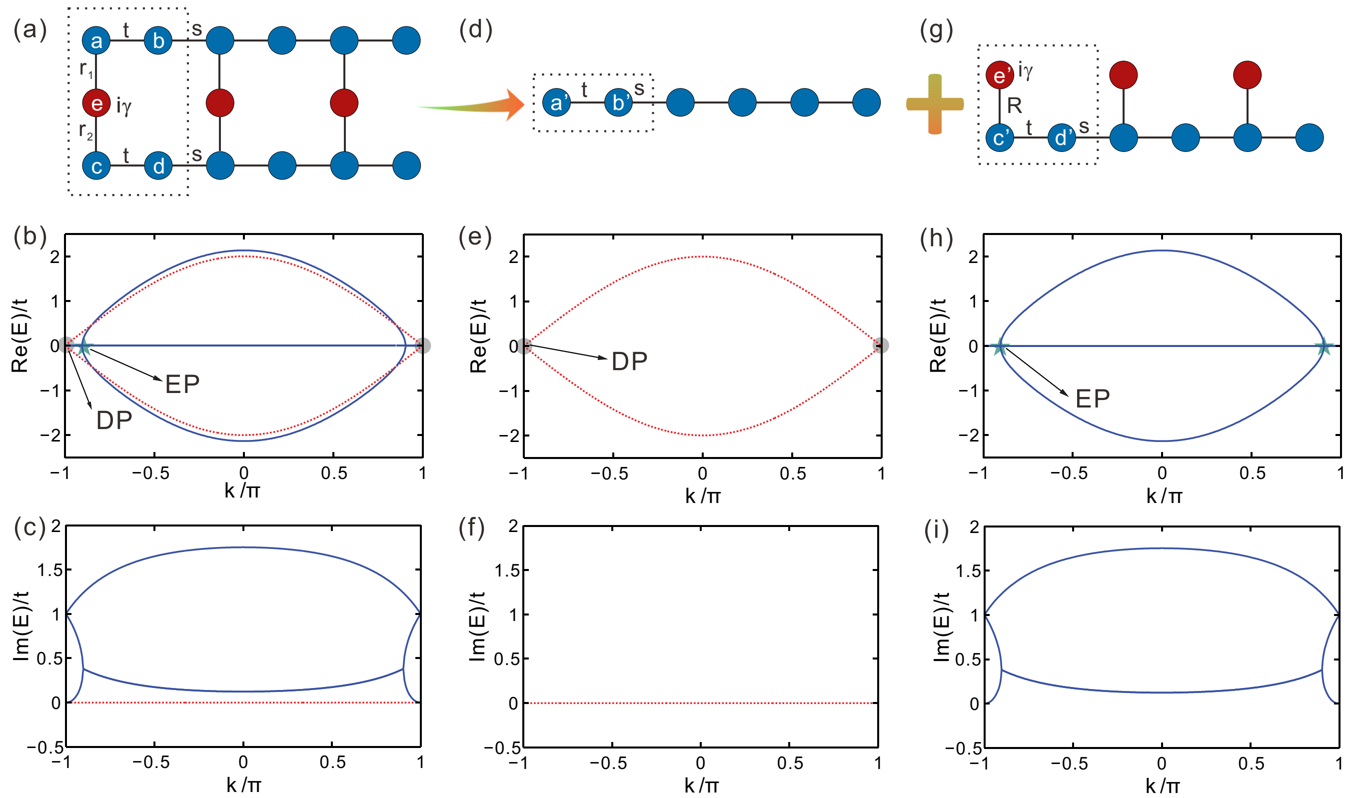

FIG. 1. Schematic of the non-Hermitian tight-binding model and band structures. (a) The proposed lattice composed of two identical SSH (blue) chains is connected by a lossy site (red) per unit cell. (b,c) are the real and imaginary parts of band structures in the entire system with $t = s = 1$, $r_1 = r_2 = \sqrt{2}/2$, and $\gamma = 2$. (d,g) are the two subspaces, corresponding to a virtual Hermitian SSH lattice and a virtual non-Hermitian Lieb lattice, respectively. (e,f) are the real and imaginary parts of band structures in a SSH chain with $t = s = 1$. (h,i) show $\mathrm{Re}(E)$ and $\mathrm{Im}(E)$ in the Lieb lattice with $t = s = 1$, $R = 1$, and $\gamma = 2$.

The existence of Hermitian subspace yields nondissipative wave dynamics, which can be utilized for creating coherent splitters that have locked phase and amplitudes at corresponding sites. Finally, we provide a feasible experimental design by exploiting optical coupled waveguides with performing full wave simulation.

II. COEXSISTENCE OF DIRAC AND EXCEPTIONAL POINTS

Figure 1(a) schematically shows the proposed tight-bind -ing model with each unit cell containing five sites labeled with symbols a–e. The quasi-one-dimensional (1D) lattice can be regarded as two equivalent SSH chains indirectly coupled through an additionally lossy chain with on-site dissipation $i\gamma$. The intra- and intercell couplings in the upper and lower chains are identical, which are marked as t and s, respectively. The couplings between the connected lattice sites and two SSH chains are signified by r_1 and r_2. Then, the Hamiltonian in real space is given by

$$H = \sum_n [t(a_n^\dagger b_n + c_n^\dagger d_n) + s(b_n^\dagger a_{n+1} + d_n^\dagger c_{n+1}) + r_1 a_n^\dagger e_n + r_2 c_n^\dagger e_n + \mathrm{H.c.}] + \sum_n i\gamma e_n^\dagger e_n. \quad (1)$$

This model was previously used in a Hermitian case to manipulate spectra of bound and bulk modes to generate the bound state in the continuum [57]. The Bloch Hamiltonian in the momentum space is figured out by using Fourier transformation, which reads as

$$H(k) = \begin{pmatrix} 0 & t + se^{-ik} & 0 & 0 & r_1 \\ t + se^{ik} & 0 & 0 & 0 & 0 \\ 0 & 0 & 0 & t + se^{-ik} & r_2 \\ 0 & 0 & t + se^{ik} & 0 & 0 \\ r_1 & 0 & r_2 & 0 & i\gamma \end{pmatrix}, \quad (2)$$

with k representing the Bloch momentum. The system is non-Hermitian in the sense that $H^\dagger(k) \neq H(k)$ with nonvanished on-site loss $i\gamma$, which dramatically hosts real and complex band structures at the same time. We show one typical case as the parameters are chosen as $t = s = 1$, $r_1 = r_2 = \sqrt{2}/2$, and $\gamma = 2$. Figures 1(b) and 1(c) plot the real and imaginary parts of the band structures, respectively. There are a total of five energy bands in the system. The two dashed red lines are a real band in the entire Brillouin zone; they linearly touch each other at $k = \pm\pi$, implying the appearance of DPs (gray filled circles). In addition, the system also supports three complex energy bands plotted by blue dotted lines. The EPs (green stars) appear in pairs at $k_{\mathrm{EP}} \approx \pm 0.91\,\pi$, which are the branch points of band structures with two band of $\mathrm{Re}(E)$ and $\mathrm{Im}(E)$ coalescing at the same time. $\mathrm{Re}(E)$ becomes degenerate and flat outside two EPs ($|k| > |k_{\rm EP}|$) and dispersive inside them ($|k| < |k_{\rm EP}|$). In contrast, two band of $\mathrm{Im}(E)$ are degenerate as $|k| < |k_{\rm EP}|$ and separated as $|k| > |k_{\rm EP}|$. The system also supports a third band with flat $\mathrm{Re}(E)$ and maximum $\mathrm{Im}(E)$ through the whole Brillouin zone. This flat band also collapses with another band at $k = \pm\pi$ under the parameters we choose, giving rise to another pair of EPs which are not discussed in detail. Therefore, the proposed system simultaneously permits the emergence of DPs and EPs.

The coexistence of two kinds of degeneracies can be well explained by block diagonalizing the Hamiltonian $H(k)$ using transformation $H_B(k) = U^{-1}H(k)U$. Then, we arrive at

$$H_B(k) = \begin{pmatrix} 0 & t+se^{-ik} & 0 & 0 & 0 \\ t+se^{ik} & 0 & 0 & 0 & 0 \\ 0 & 0 & 0 & t+se^{-ik} & R \\ 0 & 0 & t+se^{ik} & 0 & 0 \\ 0 & 0 & R & 0 & i\gamma \end{pmatrix}, \tag{3}$$

with the transfer matrix given by

$$U = \frac{1}{R}\begin{pmatrix} -r_2 & 0 & r_1 & 0 & 0 \\ 0 & -r_2 & 0 & r_1 & 0 \\ r_1 & 0 & r_2 & 0 & 0 \\ 0 & r_1 & 0 & r_2 & 0 \\ 0 & 0 & 0 & 0 & R \end{pmatrix}, \tag{4}$$

and $R = (r_1 + r_2)^{1/2}$. The upper left 2×2 and lower right 3×3 matrixes are completely decoupled from each other because the coupling between them is vanished. Consequently, the original system can be separated into two virtual subsystems $H_{\rm SSH}$ and $H_{\rm Lieb}$, corresponding to a Hermitian SSH lattice ($H_{\rm SSH}^{\dagger} = H_{\rm SSH}$) and a non-Hermitian Lieb lattice ($H_{\rm Lieb}^{\dagger} \neq H_{\rm Lieb}$), which are illustrated in Figs. 1(d) and 1(g), respectively. When $r_1 = 0$, the upper SSH chain is surely decoupled from the two lower chains. However, they are the two chains on the basis of real sites $|a\rangle, |b\rangle, |c\rangle, |d\rangle, |e\rangle$, not the two decoupled subsystems we refer to here. In fact, the transfer matrix U will change the basis of the Hamiltonian. The basis of the transferred Hamiltonian $H_{\rm B}$ is virtual supersites $|a'\rangle, |b'\rangle, |c'\rangle, |d'\rangle, |e'\rangle$. The two kinds of basis are linearly dependent on each other.

The concept of subspace was previously utilized to implement bound states in the continuum [57], the square root of topological insulators [58–62], and the coexistence of extended and Anderson localized states in the presence of disorders [63]. Here, we show the two subsystems independently support DPs and EPs, which are transparent, by calculating their eigenvalues. The eigenvalues of $H_{\rm SSH}$ are $E_{\rm SSH}^{\pm} = \pm\sqrt{t^2 + s^2 + 2ts\cos(k)}$. The DPs take place at the Brillouin edge ($k = \pm\pi$) as $t = s$, as shown in Figs. 1(e) and 1(f). The eigenvalues of the virtual Lieb lattice are plotted in Figs. 1(h) and 1(i), which are the same as that of the complex bands in Figs. 1(b) and 1(c) with EPs appearing at $k = \pm k_{\rm EP}$. Specifically, the coupling in the Lieb lattice is not independent of that in the SSH chain, while the on-site dissipation is independent. Consequently, we can adjust the dissipation to achieve EPs after DPs are prepared. The transformation between H and $H_{\rm B}$ does not change the eigenvalues, but rotates the eigenvectors. The band structures of the entire system are a direct combination of two Hermitian and non-Hermitian subsystems. Moreover, as the matrix U is unitary ($U^{\dagger} = U^{-1}$), the orthogonality of eigenvectors remains unchanged after transformation. Therefore, the entire system inherits the nature of the Hermitian and non-Hermitian subspaces, allowing the coexistence of DPs and EPs.

Whether the energy bands are Hermitian or not can be further verified by calculating the phase rigidity of the respective bands, defined as

$$p_n(k) = \left|\frac{\langle \Psi_n(k)|\,\Phi_n(k)\rangle}{\langle \Phi_n(k)|\,\Phi_n(k)\rangle}\right|. \tag{5}$$

$\langle \psi_n(k)|$ and $|\Phi_n(k)\rangle$ denote the left and right eigenvectors of the nth energy band at momentum k, which satisfy $H^{\dagger}(k)|\Psi_n(k)\rangle = E_n^*(k)|\Psi_n(k)\rangle$ and $H(k)|\Phi_n(k)\rangle = E_n(k)|\Phi_n(k)\rangle$, respectively. Phase rigidity characterizes the mixture of different states. At EPs, the two states are perfectly mixed as a result of the collapse of the eigenvectors, resulting in vanished phase rigidity. In contrast, phase rigidity is unitary when the system is Hermitian. As shown in Fig. 2(a), we plot the phase rigidity of each band as a function of Bloch momentum. The first and second bands remain unitary throughout the Brillouin zone, implying their Hermitian nature. Therefore, the degeneracies at $k = \pm\pi$ are Hermitian DPs. In contrast, one can see $p_3 = p_5 = 0$ at $k \approx 0.91\,\pi$, indicating the appearance of EPs. By the way, we also have EPs as $p_4 = p_5 = 0$ at $k \approx \pi$, which is consistent with the discussions about Fig. 1. To sum up, we have constructed a non-Hermitian system hosting DPs and EPs at the same time, which stem from the coexistence of Hermitian and non-Hermitian subspaces.

The decomposition of the whole system into a Hermitian and a non-Hermitian subsystem may be explained by pseudochirality, which is also referred to as non-Hermitian chiral symmetry or pseudo-anti-Hermitian symmetry [16,32,64],

$$U_{\rm PC}H(k)U_{\rm PC}^{-1} = -H\dagger(k), \tag{6}$$

with $U_{\rm PC} = \mathrm{diag}(-1, 1, -1, 1, 1)$. This symmetry leads to a constraint on eigenvalues and eigenstates as $H(k)$ $U_{\rm PC}|\Psi(k)\rangle = -U_{\rm PC}H^{\dagger}(k)|\Psi(k)\rangle = -E^*U_{\rm PC}|\Psi(k)\rangle$. This indicates $U_{\rm PC}|\Psi(k)\rangle$ is also an eigenstate of H with eigenvalues of $-E^*$. As a result, the eigenvalues are either purely imaginary numbers (symmetric phase) or occur in pairs () (broken phase). Furthermore, the conjugate pair allows two different conditions with $E_1 = a$, $E_2 = -a$ or $E_3 = a + bi$, $E_4 = -a + bi$, a, $b \in \mathrm{R}$. For our five-band non-Hermitian system, the more specific situation is listed in Table I.

The pseudochirality permits a subspace with two real eigenvalues, which may be Hermitian on the condition that the associated eigenvectors are orthonormal to each other, $\langle\Phi_1|\Phi_2\rangle$=$\langle\Phi_1|U_{\text{or occur in pairs}}|\Psi_1\rangle$= 0, or the left and right eigenstates belonging to the same eigenvalues are equal, $|\Phi_{1,2}\rangle$=$|\Psi_{1,2}\rangle$. We now show this subspace is indeed a Hermitian one according to the rank-nullity theorem argument [57], which indicates there must be a Hermitian SSH subsystem. When the interchain coupling ($r_1 = r_2 = 0$) is absent, the system supports two degenerate bands similar to SSH chains

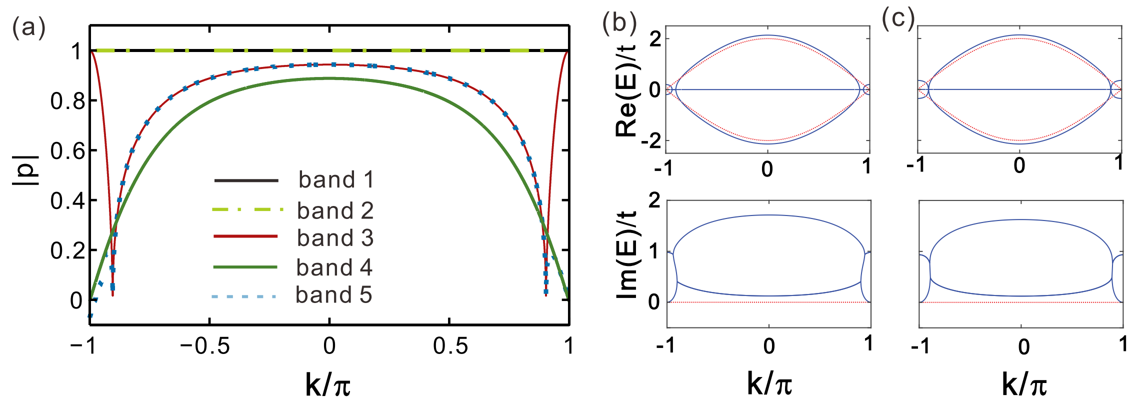

FIG. 2. Phase rigidity and third-order exceptional points. (a) Phase rigidity for different band structures corresponding to Fig. 1. (b,c) are the real (upper panel) and imaginary parts (lower panel) of band structures for different on-site loss. (b) $\gamma = 1.96i$. (c) $\gamma = 1.84i$. Other parameters are kept unchanged compared to Fig. 1.

$E^{\pm}_{\rm SSH}$. Then, after a transformation, the Hamiltonian in the basis of eigenvalues reads as

$$h(k) = X^{-1}H(k)X$$
$$= \begin{pmatrix} E^{+}_{\rm SSH} & 0 & 0 & 0 & \frac{r_1\rho^*}{\sqrt{2}} \\ 0 & E^{+}_{\rm SSH} & 0 & 0 & \frac{r_2\rho^*}{\sqrt{2}} \\ 0 & 0 & E^{-}_{\rm SSH} & 0 & -\frac{r_1\rho^*}{\sqrt{2}} \\ 0 & 0 & 0 & E^{-}_{\rm SSH} & -\frac{r_2\rho^*}{\sqrt{2}} \\ \frac{r_1\rho}{\sqrt{2}} & \frac{r_2\rho}{\sqrt{2}} & -\frac{r_1\rho}{\sqrt{2}} & -\frac{r_2\rho}{\sqrt{2}} & i\gamma \end{pmatrix}, \quad (7)$$

where

$$X = \frac{1}{\sqrt{2}}\begin{pmatrix} \rho & 0 & -\rho & 0 & 0 \\ 1 & 0 & 1 & 0 & 0 \\ 0 & \rho & 0 & -\rho & 0 \\ 0 & 1 & 0 & 1 & 0 \\ 0 & 0 & 0 & 0 & \sqrt{2} \end{pmatrix}, \quad (8)$$

and $\rho = (t + se^{-ik})/E^{+}_{\rm SSH}$. The two terms $E^{\pm}_{\rm SSH}$ are coupled to the lossy site $i\gamma$ with $C_+ = (r_1\rho, r_2\rho)/\sqrt{2}$ and $C_- = -(r_1\rho, r_2\rho)/\sqrt{2}$. It is easy to find two eigenvectors of the Hamiltonian $h(k)$; that is, $|\Phi^+\rangle = (\phi_1 \quad \phi_2 \quad 0 \quad 0 \quad 0)^T$ and $|\Phi^-\rangle = (0 \quad 0 \quad \phi_3 \quad \phi_4 \quad 0)^T$ with eigenvalues $E = E^{\pm}_{\rm SSH}$. It is obvious that the two eigenvectors are also orthogonal to each other; namely, $\langle\Phi^+|\Phi^-\rangle = 0$. Consequently, the proposed indirectly coupled SSH chain always sustains a set of Hermitian SSH bands regardless of the loss present in the immediate chain. More physically, the rank of $C_\pm$ indicates the effective coupling channels to other parts [57]. There is only one channel present in the system such that only one set of $E = E^{\pm}_{\rm SSH}$ is lifted and the other set survives. To sum up, our proposed non-Hermitian system always sustains a Hermitian SSH subsystem.

TABLE I. The eigenvalues E of the five sites non-Hermitian system.

PC-symmetric phase	PC-broken phase
$E_1 = -E_2,\ E_{1,2} \in R$	$E_1 = -E_2, E_{1,2} \in R$
$E_{3,4} \in iR$	$E_3 = -E^*_4$
$E_5 \in iR$	$E_5 \in iR$

We also discuss the symmetry of two decoupled subsystems, namely, the virtual SSH and non-Hermitian Lieb chains. The SSH chain has chiral symmetry $\sigma_z H_{\rm SSH}(k)\sigma_z^{-1} = -H_{\rm SSH}(k)$ with σ_z denoting the Pauli matrix. This symmetry leads to the appearance of paired eigenvalues $(E, -E)$, quantized Zak phase, and zero-energy topological edge modes in the SSH chains. On the other hand, the virtual Lieb lattice also respects PC symmetry, $\Gamma_{\rm PC}H_{\rm Lieb}(k)\Gamma^{-1}_{\rm PC} = -H^{\dagger}_{\rm Lieb}(k)$, with $\Gamma_{\rm PC} = {\rm diag}(1, -1, -1)$. In addition to leading to paired eigenvalues $(E, -E^*)$, this symmetry promises the stable EP3 in two dimensions composed of parameter space. According to [64], we construct a characteristic polynomial, $P_\lambda = \det[H_{\rm Lieb}(\lambda) - E]$. EP3 appears when the determinant of the first- and second-order resultant vector are vanished, that is, $R_j(\lambda_0) = (-i)^{n(n-j)}R_{P,P^{(j)}}$. By solving the equation, we can figure out the condition for EP3:

$$\gamma = \pm 3\sqrt{3}\sqrt{t^2 + s^2 + 2ts\cos k},$$
$$R = \pm 2\sqrt{2}\sqrt{t^2 + s^2 + 2ts\cos k}. \quad (9)$$

As $t = s$, Eq. (9) reduces to $k = \pm \arccos(\frac{r^2}{16t^2} - 1)$, $\gamma = \pm \frac{3\sqrt{3}R}{2\sqrt{2}}$. Figures 2(b) and 2(c) plot the numerical band structures as $t = s$ for different on-site dissipation. As γ increases, the two EP2's get closer. At $\gamma = 1.84$, they collapse into EP3 at $k = \pm 0.89\pi$, accommodated with the condition indicated by Eq. (9).

III. NONDISSIPATIVE WAVE DYNAMICS

Now we show that the characteristics of Hermitian and non-Hermitian subspaces can be reflected from wave dynamics by suitably choosing an initial wave packet to stimulate them. The state at time t_f relates to initial state t_i as $|\Phi_{t_f}\rangle = T\exp[-i\int_{t_i}^{t_f} Hdt]|\Phi_{t_i}\rangle$ with T denoting the time ordering product. We use the Crank-Nicolson approximant to calculate the time-evolution operator

$$\exp[-iH\Delta t] = \frac{1 - iH\Delta t/2}{1 + iH\Delta t/2} + O(\Delta t^3). \quad (10)$$

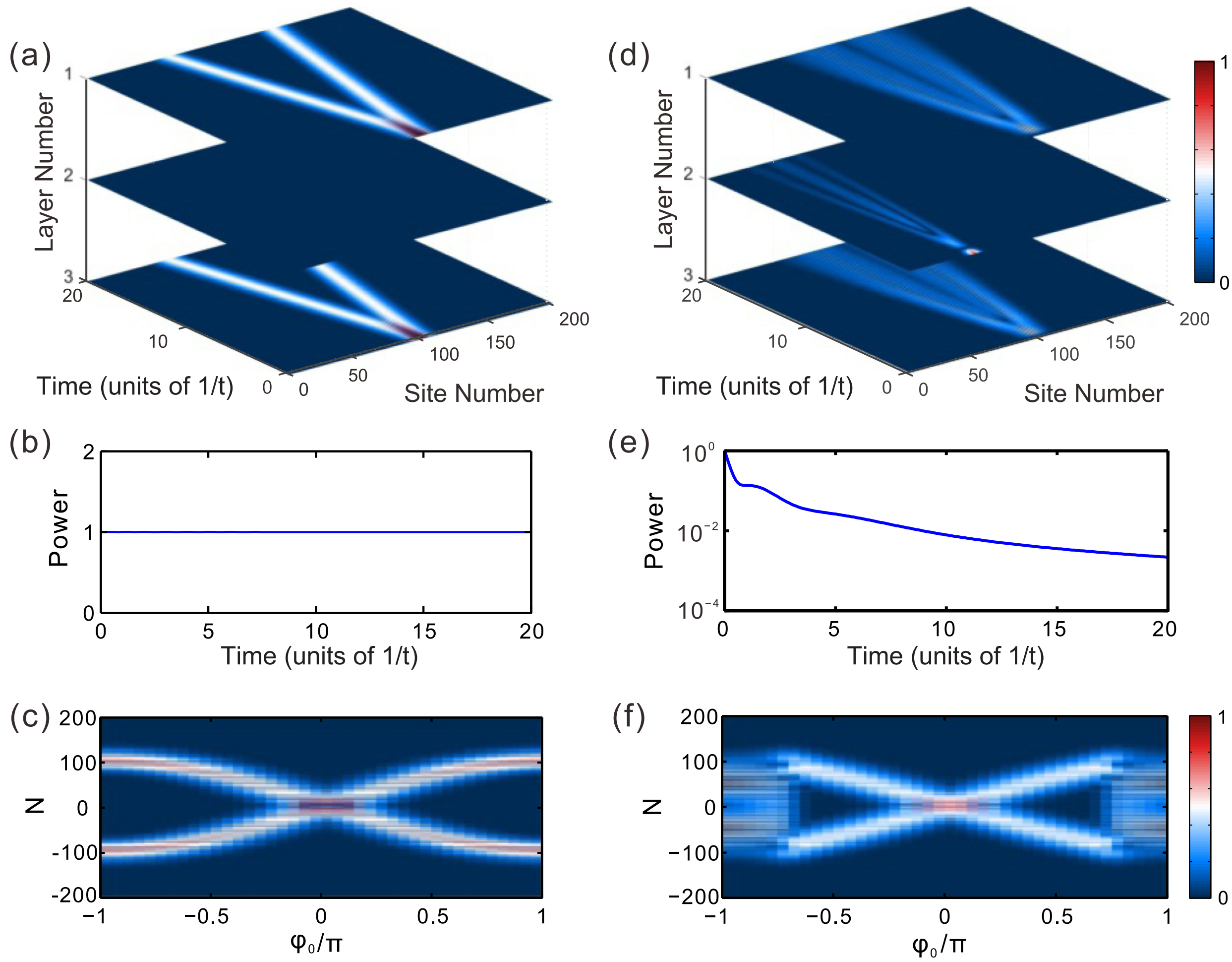

FIG. 3. Wave dynamics for Hermitian and non-Hermitian subspaces. (a–c) are for the Hermitian subspace as waves are launched from the two upper and lower layers at the same time. (a) shows the field intensity for beam excitation as $\varphi_0 = \pi$, where φ_0 denotes the phase difference between adjacent sites. (b) plots the evolution of total power corresponding to (a). (c) shows the output field distributions as φ_0 is varying. (d–f) are for non-Hermitian subspaces with waves launched from the middle lossy layer. In all cases, the Gaussian width of the beam envelope is $w_0 = 20$.

Then the wave propagation in time can be numerically figured out according to the coupled mode equation. In Fig. 3 , we launch wave beams from sites a and c with opposite amplitudes (upper and lower two layers) under a Gaussian packet given by $a_n = r_2 e^{-n^2/w_0^2} e^{in\varphi_0}$ and $c_n = -r_1 e^{-n^2/w_0^2} e^{in\varphi_0}$, where φ_0 and w_0 are the initial phase difference and beam width, respectively. The phase difference is to arouse the Bloch mode near $k = \varphi_0$. In this way, the virtual SSH chain is excited since the supersites between SSH and original lattices are related as

$$|a'\rangle = (-r_2|a\rangle + r_1|c\rangle)/R,$$
$$|b'\rangle = (-r_2|b\rangle + r_1|d\rangle)/R. \qquad (11)$$

Figure 3(a) shows the wave evolution as the initial phase difference of the wave packet is $\varphi_0 = \pi$. The beam width is fixed at $w_0 = 20$. The wave propagation direction is determined by the group velocity and is figured out to be $\theta(\varphi_0) = -\arctan(\partial E/\partial k)$ [65]. At $\varphi_0 = \pi$, the Bloch modes around the DPs are stimulated where the energy bands of SSH are approximated to be $E \approx \pm t(\pi - k)$. The band structure is linear in the vicinity of the DPs and the group velocity is not certainly defined due to the intersection of two band structures. As a result, light splits into two beams with a fixed beam width, as shown in Fig. 3(a), where the self-splitting phenomenon appears in both the first and third layers without any energy residing in the middle lossy layer. In addition, the total power of the system remains constant during the propagation, as depicted in Fig. 3(b). We further illustrate the output intensity profiles as a function of the phase difference of the initial wave packet in Fig. 3(e). The output profiles display a sinusoidal curve, fairly coincident with the cosine feature of band structures of the SSH model. By selectively stimulating different sites at the initial condition, we present the self-splitting and collimated beam propagations, which correspond to the typical characteristics of DPs and EPs, respectively. According to Eq. (11), the Hermitian counterpart can also be stimulated if waves are injected from sites b and d with opposite amplitudes and also from the four sites with the proper combination.

We now launch waves from the lossy sites e from the middle layer with a Gaussian envelope to stimulate the non-Hermitian subspace. The supersites of the virtual Lieb lattice

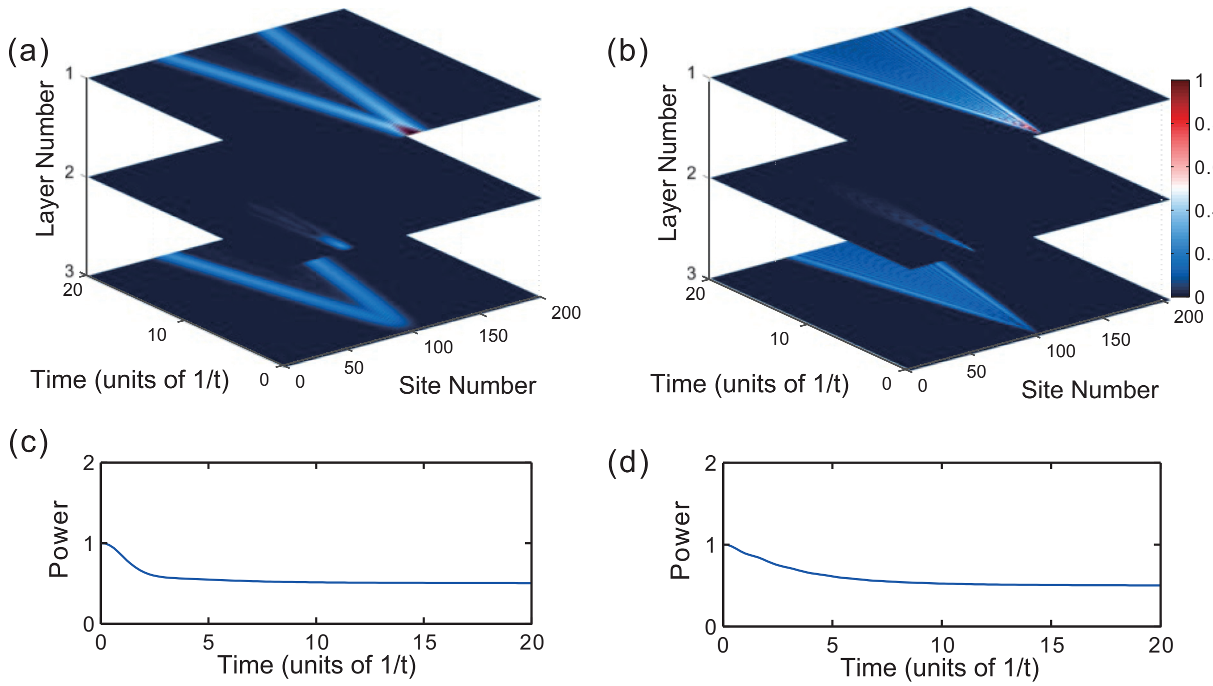

FIG. 4. Nondissipative wave dynamics via Hermitian subspace where waves are illuminated from the upper layer. (a) is the field intensity for the excitation of Gaussian beam with phase difference $\varphi_0 = \pi$. (b) is the field intensity for single-site excitation. (c,d) are the evolution of total power corresponding to (a,b), respectively. Other parameters are the same as that used in Fig. 3.

relate to the original model as

$$\begin{aligned} |c'\rangle &= (r_1|a\rangle + r_2|c\rangle)/R, \\ |d'\rangle &= (r_1|b\rangle + r_2|d\rangle)/R, \\ |e'\rangle &= |e\rangle. \end{aligned} \tag{12}$$

The virtual supersite $|e'\rangle$ is the same as the real site $|e\rangle$. In this case, only the virtual non-Hermitian Lieb lattice is excited. We plot one typical wave propagation $\varphi_0 = \pi$, as shown in Fig. 3(d). The intensity is normalized to clearly present the intensity distribution. Since the group velocity is zero, the center of the beam remains unchanged during the evolution, in contrast to the split beams of the Hermitian case as $\varphi_0 = \pi$. On the other hand, the total energy for this excitation exponentially decreases, clearly demonstrating its non-Hermitian characteristics, as shown in Fig. 3(e). Furthermore, EPs can be probed from the evolution profiles. As illustrated in Fig. 3(f), we plot the output intensity profiles, as the evolution time is 20(units of $1/t$), as a function of the phase difference of the initial wave packet. On the edge of the Brillouin zone, the real part of the band structure is flat outside the two EPs, resulting in collimated propagation, and thus the center of the output fields remains at the center. Within the range of two EPs, the waves split into two separated beams except $\varphi_0 = 0$. The output profiles exhibit distinct boundaries, which are differentiated by EPs.

The coexistence of Hermitian and non-Hermitian subspaces raises a significant physical consequence, giving rise to stable and nondissipative wave dynamics that has locked phase and amplitudes at two SSH layers. Figures 4(a) and 4(b) show the wave propagations for beam and single-site injections, respectively. In both cases, the waves are launched from the upper layer. Other parameters stay unchanged, as that used in Fig. 3. For the injection of the Gaussian beam with phase difference $\varphi_0 = \pi$, waves split into two beams without diffraction at the upper layer [Fig. 4(a)]. At the same time, a similar image as the upper layer is automatically formed at the lower layer. For single-site injection, we also see two similar patterns (known as discrete diffraction) formed at upper and lower layers [Fig. 4(b)]. This self-imaging phenomenon is a result of the existence of Hermitian subspace. In Figs. 4(c) and 4(d), we plot the total energy versus time corresponding to Figs. 4(a) and 4(b). In both cases, the energy decreases first and then remains stable without decay. Considering the Hermitian and non-Hermitian subspaces are completely decoupled, an injection will result in definite amounts of energy in respect to the two subsystems. The energy in the non-Hermitian subsystem will be completely decayed without affecting the amount of energy in the Hermitian subspace. As a result, the total energy will become stable after long enough evolution [Figs. 4(c) and 4(d)]. In addition, a supersite of a virtual Hermitian subspace relates to two real sites according to Eq. (11). Hence, the waves at corresponding sites in the upper and lower layers always differ by a phase π and their amplitudes are determined by the relation between supersites and real sites, which can be further controlled by interchain couplings r_1 and r_2.

IV. TOPOLOGICAL EDGE MODES

The coexistence of two subspaces furthermore enables the investigation of Hermitian and non-Hermitian topological edge modes in a single system. The topological property of the whole system originates from its two virtual subsystems, which bulk-edge correspondence inherits that from the virtual Hermitian SSH model and the non-Hermitian Lieb lattice. The

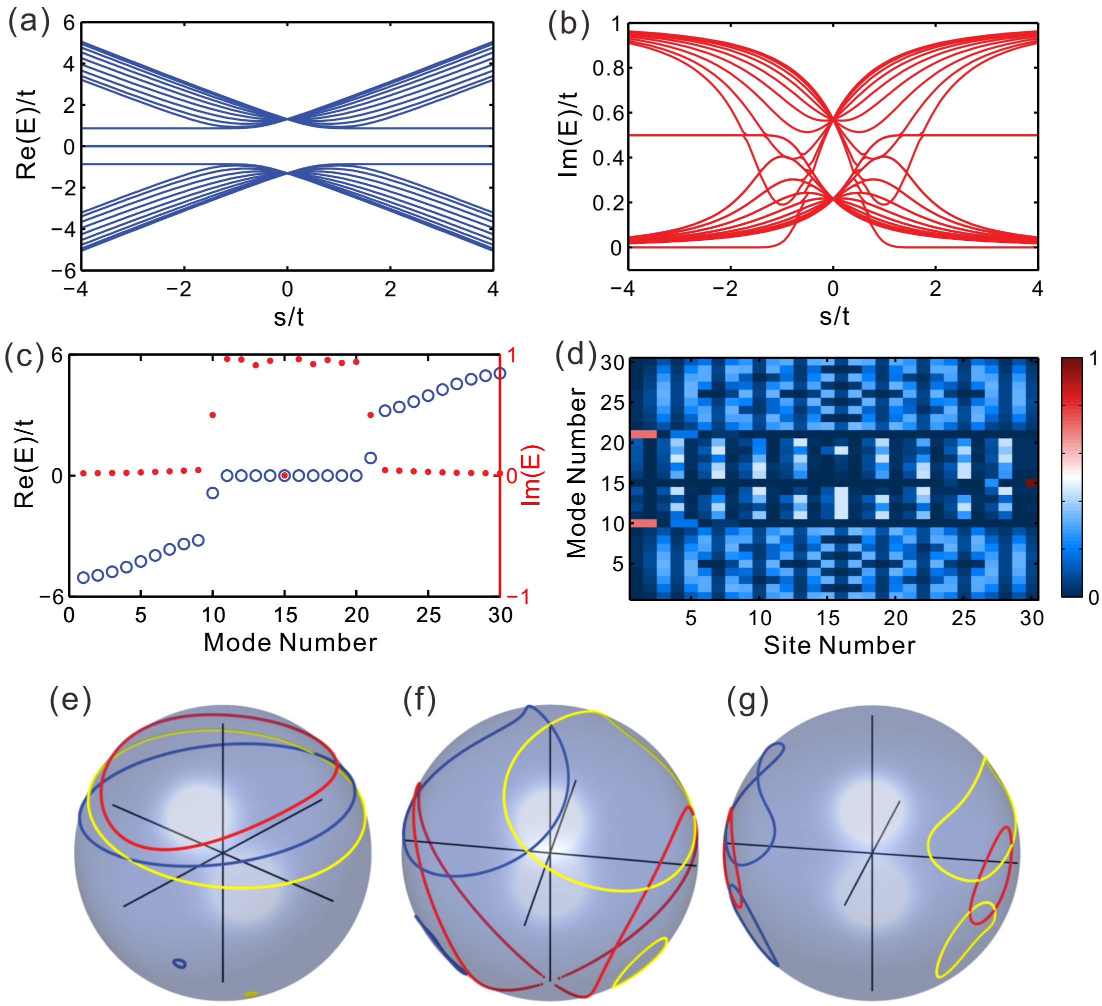

FIG. 5. The bulk-edge correspondence of the virtual Lieb lattice using MSR. (a,b) are the real and imaginary parts of the energy spectrum for a finite chain as a function of coupling s, respectively. We set $t = 1$, $R = 1$, and $\gamma = 1$. (c) The eigenvalues of supermodes in nontrivial phase ($t = 1$, $s = 4$). The blue circles and red dots represent Re(E) and Im(E), respectively. (d) Mode profiles plotted as a function of mode number. (e–g) are MSs on Bloch spheres in the topological, transition, and trivial phases.

standard Hermitian SSH model was well studied in previous works, where the topological phase transition emerges at the DPs as $t = s$. As intercell coupling exceeds intracell coupling ($t < s$), the system is in the topological nontrivial phase, supporting two zero-energy edge modes under open boundary conditions. In contrast, as $t > s$, there are no edge modes under open boundary conditions because the system is in the trivial phase.

We now study the bulk-edge correspondence for the Lieb lattice based on MSR. The results show that the topological phase transition is only determined by the relative value of coupling of t and s, irrespective of interchain coupling r_1, r_2 or on-site loss. In Figs. 5(a) and 5(b), we plot the eigenvalue spectra of the Lieb lattice as coupling s is varied. Other parameters are fixed at $t = 1$, $R = 1$, $\gamma = 1$ and the total number of sites is $N = 30$. As $s/t > 1$, a pair of edge modes appears in the upper and lower band gaps of Re(E). For the parameters given in Fig. 5, their eigenvalues are $E = \pm 0.866 + 0.5i$. In addition, there is always a flat band in the real part of the spectrum, which further supports a topological edge mode with zero energy as $s/t > 1$. To clearly see edge modes, we plot the eigenvalues for the open chain in the nontrivial phase as $s/t = 4$. The two modes with $E = \pm 0.866 + 0.5i$ (mode number $N = 10$ and 21) reside in the band gap. An edge mode with energy $E = 0$ (mode number $N = 15$) lies in the flat band, which can be distinguished from their imaginary part of the energy. In addition, the edge modes can also clearly be reflected from distributions of mode profiles, as shown in Fig. 5(d) where the tenth and 21st modes are confined at the left edge and the 15th mode resides at the right termination.

We now utilize MSR to reveal the bulk-edge correspondence of this non-Hermitian Lieb lattice by mapping the eigenstates of a Bloch Hamiltonian as a set of stars on Bloch sphere. The Majorana stars are determined by a polynomial equation for the complex variable x [55,56],

$$\sum_{l=0}^{2L} \frac{(-1)^l C_{2L-l+1}}{\sqrt{(2L-l)!l!}} x^{2L-l} = 0, \tag{13}$$

where $L = (n–1)$ with n denoting the number of energy bands; C_i represents the component of the right eigenvec-

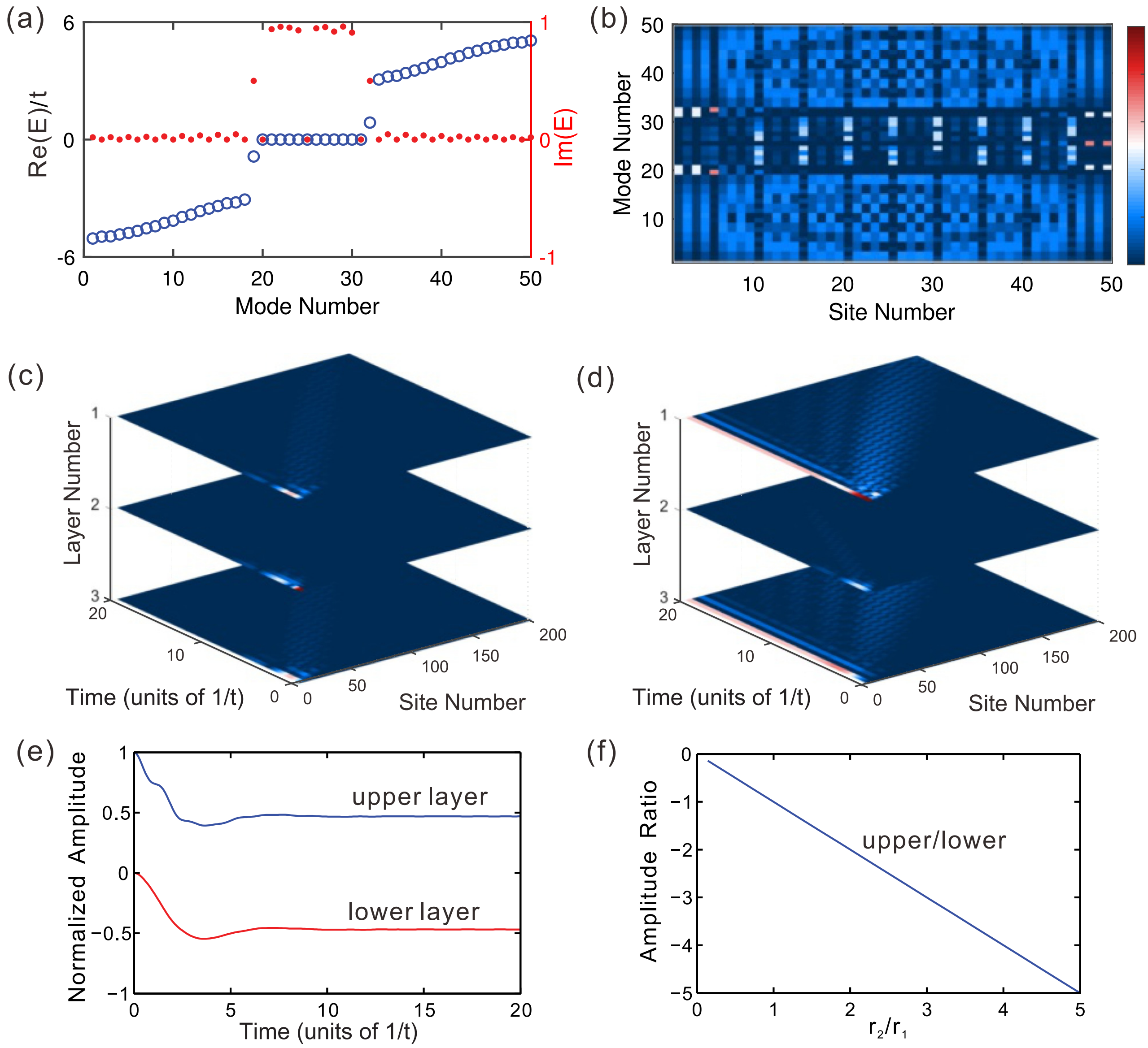

FIG. 6. Topological edge modes in the whole systems and their evolution. (a,b) are the eigenvalue spectra and field distributions, respectively. The parameters are $t = 1$, $s = 4$, $r_1 = r_2 = \sqrt{2}/2$, and $\gamma = 1$. (c,d) are the evolution of edge modes where the waves are launched from (c) the left lossless site a and (d) the left lossy site e from the upper layer. (e) plots the time-varying amplitudes at the first site at the upper and lower layers. (f) plots the ratio of output amplitude of the upper layer to that of the lower layer as interlayer coupling is varied. The total evolution time is set to be $t = 20$.

tors, $|\Phi_n\rangle = [C_1 \quad C_2 \quad \cdots \quad C_i]^T$. For our three-band ($n = 3$) system, we get two roots of x and then determine two Majorana stars (MSs) according to $x = \tan(\theta/2)\exp(i\phi)$ with $(1, \theta, \phi)$ signifying the coordinates on the Bloch sphere. By continuously varying Bloch momentum k, we arrive at full representation of the MS, which generally forms a closed loop.

The different topological phases can be directly viewed through MSR depending on whether they encircle the z axis that connects the north and south poles. Figures 5(e) and 5(f) show three typical cases of MSR for different couplings s. In the topologically nontrivial phase as $s > t$, there are three loops encircling the z axis [Fig. 5(e)]. At the transition point, we see some loops just pass through the north or south poles [Fig. 5(d)]. In the trivial phase as $s < t$, all loops exclude the z axis. The topological invariant can be defined by the azimuthal winding number of each energy band [55]:

$$\upsilon = -\frac{1}{2\pi}\sum_{m=1}^{2}\oint \partial_k\phi_m(k)dk, . \tag{14}$$

The number of topological edge modes under open boundary conditions is equal to the summation of all winding numbers. In the Lieb chain, the total winding number $\upsilon_a = 3$ as three loops encircle the z axis in the nontrivial phase, equaling the number of edge modes. Therefore, the phase transition point and the number of edge modes are indicated by MSR, constructing the bulk-edge correspondence in our system.

The above discussions show that both virtual subsystems experience topological phase transition at $t = s$. Then we can

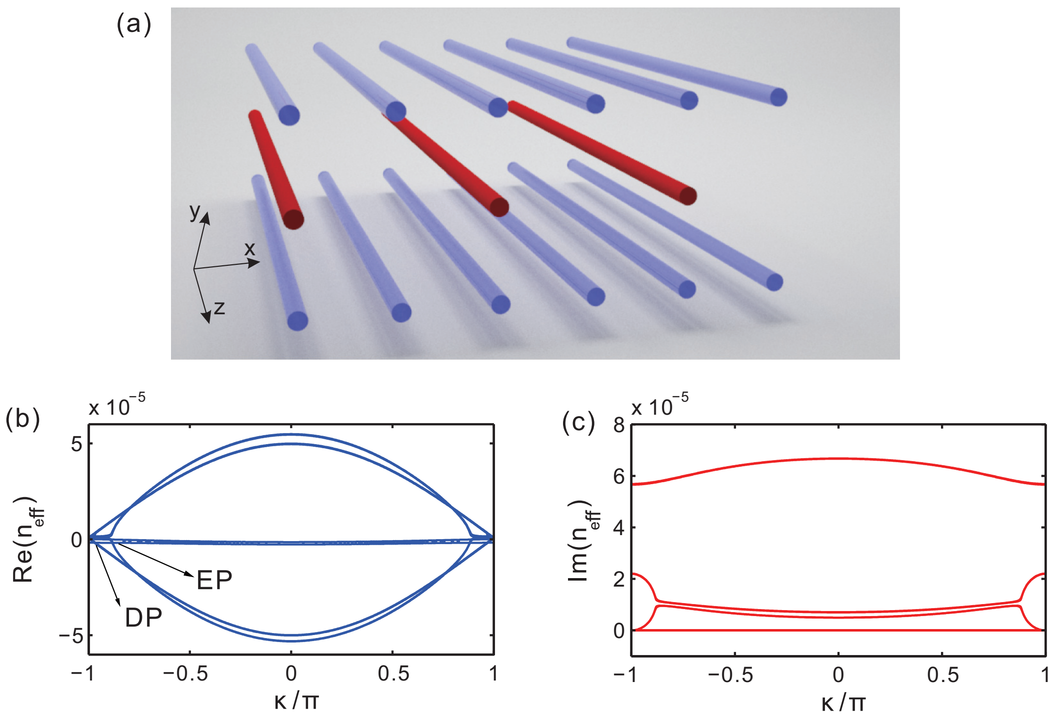

FIG. 7. Simulation of the proposed model using a coupled waveguide array. (a) The schematic of geometry of waveguide arrays. (b,c) are simulated real and imaginary parts of band structures. In the simulation, the parameters are $\lambda = 1.55\,\mu$m, $n_0 = 3.5$, $d_x = d_y = 7\,\mu$m, $n_0 = 3.5$, $n_{\rm core} = 3.52$, and ${\rm Im}(n_{\rm core}) = 1.15 \times 10^{-4}$.

easily figure out the topological property of the total system, whose phase transition point is also $t = s$ and supports five edge modes, the summation of the number of edge modes in the two subsystems. In Fig. 6(a), we plot the eigenvalues for the open chain in the nontrivial phase as $t < s$. The total number of lattice sites is $N = 50$. The spectrum hosts two dispersive energy bands with a vanished imaginary part of eigenvalues. We can also see a lossy band with flat ${\rm Re}(E)$ isolated from the dispersive bands. Figure 6(b) shows the field distributions of all modes, arranged by the real part of the energy. There are five topological edge modes supported in the system. Two edge modes with $E = 0$ ($N = 20$ and 31) stem from the Hermitian subspace, which are localized at both sides of the system due to chiral symmetry. In addition, there is another set of edge modes originating from the virtual Lieb lattice. The spatial profile of the zero-energy edge mode ($N = 25$) is accumulated at the right boundary and has vanished amplitudes residing on lossy sites. The other two modes with $E = \pm 0.866 + 0.5i (N = 19$ and 32) are in the band gap. They are confined at the left termination of the system and some fields are distributed at lossy sites.

We now study the wave dynamics of Hermitian and non-Hermitian edge modes, which can be separately stimulated by choosing suitable initial excitation. Figures 6(c) and 6(d) present the wave evolution for different initial conditions as waves are injected from a single site. When waves are injected from the lossy site e at the left termination of the middle layer, as shown in Fig. 6(c), the two edge modes from the non-Hermitian subspace are stimulated. In this case, we observe a breathing, beating intensity profile with beating length $L = 2\pi/{\rm Re}(\Delta E_{\rm edge}) \approx 3.63$. The field intensity decreases during the evolution since these modes have imaginary parts of eigenvalues. In Fig. 6(d), we launch waves from the left site a in the upper layer. In this case, the two zero-energy edge modes from the Hermitian subspace are excited. We can see some waves are confined at the left edge in both of the upper and lower layers with uniform intensity while some experience diffraction during the propagation. After enough evolution time, the energy in the upper and lower two layers becomes stable without dissipation. In Fig. 6(e), we plot the amplitudes of waves at the first sites in the upper and lower two layers. It clearly shows that the amplitudes firstly decrease and then remain unchanged as the time becomes larger than 5. Since the interlayer coupling is $r_1 = r_2$, the stable amplitudes for two layers are equal with negative opposite signs, implying they are of antiphase. We refer to this phenomenon as the coherent splitters since the waves in the two layers automatically have locked phase and amplitudes that are independent of evolution time. The underlying mechanism relies on the relation between virtual supersites and real sites. According to Eq. (11), the wave amplitude of supersite $|a'\rangle$ in the Hermitian subspace leads to certain amplitudes in real sites $|a\rangle$ and $|c\rangle$ determined by interchain coupling $-r_1$ and r_2, which can be further utilized to control output amplitudes. As shown in Fig. 6(f), we plot the ratio of amplitudes between the upper and lower layers (first site) at the output (time is 20) as interchain coupling r_2 is varied. The ratio linearly increases with r_2/r_1 and the amplitudes in different layers are always out of phase.

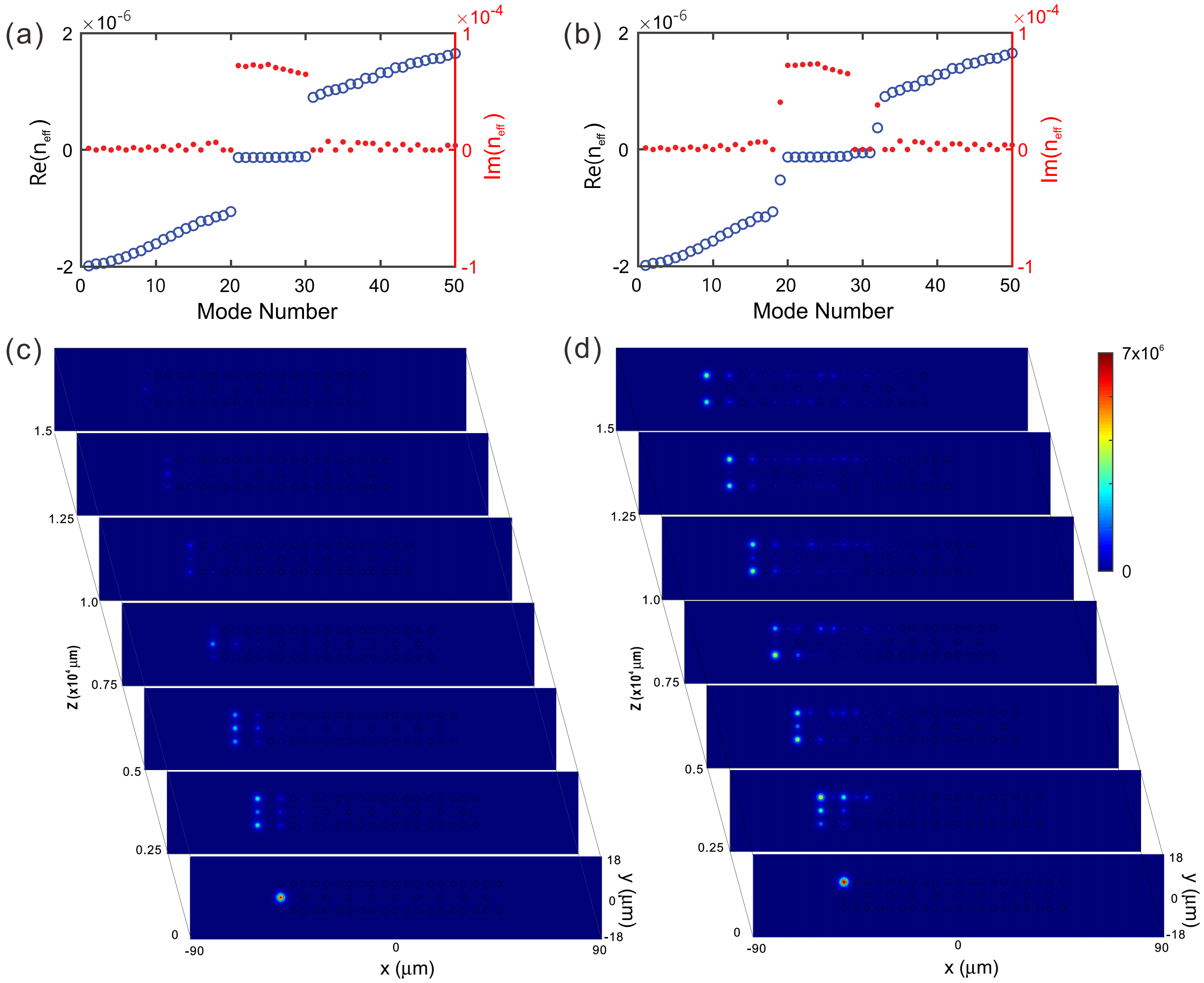

FIG. 8. Simulations of energy spectrum and edge dynamics. (a,b) show the energy spectrum of the trivial and nontrivial arrays, respectively. (c,d) are the evolution of edge states of different subspaces by exciting the e and a single sites. The parameters are $d_{x1} = 4.375\,\mu$m, $d_{x2} = 5.6\,\mu$m, $d_y = 5.775\,\mu$m in (a) and $d_{x1} = 5.6\,\mu$m, $d_{x2} = 4.375\,\mu$m, $d_y = 5.775\,\mu$m in (b–d). Other parameters are the same as in Fig. 7.

V. OPTICAL DESIGN OF WAVEGUIDE

The proposed theoretical model can be realized in coupled waveguide arrays, which are schematically shown in Fig. 7(a) with each unit cell containing five-cylinder waveguides. The light waves propagate along the z direction. The evolution of waveguides is determined by the Helmholtz equation [8,66],

$$\left[\nabla^2 + k_0^2\varepsilon(x)\right]\Phi(x, z) = 0, \tag{16}$$

where $\Phi(x, z)$ represents the field amplitude, k_0 denotes the wave vector in free space, and $\varepsilon(x)$ is the relative permittivity. In the weakly coupling regime where the spatial spacing between neighboring waveguides considerably exceeds the mode width of the single waveguide, the system is subjected to a tight-binding model [8]. In the simulation, the refractive index of the background dielectric is $n_0 = 3.5$. The radius of the cylinder waveguide is $w = 1.2\,\mu$m with refractive index $n_{\mathrm{core}} = 3.52$. The connecting waveguide at the middle row is lossy with the imaginary part of the refractive index being $\mathrm{Im}(n_{\mathrm{core}}) = 1.15 \times 10^{-4}$. We assume the incident wave is at the communication band with $\lambda = 1.55\,\mu$m. Under these parameters, the effective refraction of each individual waveguide is figured out to be $n_{\mathrm{eff}} = 3.5071$ with two degenerate ground modes which have different polarizations. All the simulations are performed in COMSOL MULTIPHYSICS. The two degenerate modes are generally uncoupled. For simplicity, we consider the array has a homogeneous spatial spacing with the spacing along the x and y directions being $d_x = d_y = 7\,\mu$m, corresponding to relative coupling strength $t = s = r_1 = r_2$. The simulated results of band structures are shown in Figs. 7(b) and 7(c), which are accommodated with the tight-binding model shown in Fig. 1. The two bands that stem from the Hermitian subspace have vanished $\mathrm{Im}(E)$, while DPs appear at the edge of the Brillouin zone ($k = \pm\pi$). We also see $\mathrm{Re}(n_{\mathrm{eff}})$ and $\mathrm{Im}(n_{\mathrm{eff}})$ of the other three complex bands almost coalesce at $k = \pm 0.89\,\pi$. The results clearly demonstrate the coexistence of DPs and EPs. Figure 8 shows us the energy spectrum of the trivial and nontrivial conditions and the intensity distributions of edge states at different propagation distances. The array comprises ten unit cells with open boundaries. The trivial arrays have an intracell distance $d_{x1} = 4.375\,\mu$m, intercell distance $d_{x2} = 5.6\,\mu$m, and the interchain distance $dy = 5.775\,\mu$m. Other parameters are the same as those in Fig. 7(b). We swap intracell distance with intercell distance in the nontrivial arrays; other parameters remain unchanged. We can see that the energy spectra in Fig. 8(b) fit well with that in Fig. 6(a). We also plot the energy spectra of the trivial arrays in Fig. 8(a) which are consistent with the numerical results. The dynamics of the boundary states at the a and e sites at the leftmost of the arrays is stimulated. We get the field distributions with a series of evolution lengths increasing gradually from 0 to 15 mm with an interval of 2.5 mm. The propagation of the edge states in Figs. 8(c) and 8(d) is consistent with that in Figs. 6(c) and 6(d), respectively. When the e site is excited, the energy decreases during the evolution and a breathing, beating phenomenon is clearly shown. When the a site is stimulated, the field intensity decreases with the propagation distance increasing until the distance arrives at 12.5 mm approximately. After this point, the energy remains equal in the a and c sites. Therefore the edge mode from the Hermitian and non-Hermitian subspaces can be stimulated by different stimulation ways.

VI. CONCLUSIONS

In conclusion, we have shown that a non-Hermitian system, which is composed of two identical SSH chains indirectly coupled through a lossy chain, can be divided into two completely decoupled virtual subsystems comprising a Hermitian SSH chain and a non-Hermitian Lieb lattice. In aid of Hermitian subspace, the system is able to sustain real spectra despite its non-Hermitian nature. Since the dissipation present in the system only affects the non-Hermitian subspace, we can engineer two subsystems independently, allowing the coexistence of DPs and EPs. The two different kinds of singular points have unique band structures near them and thus provide versatile approaches to controlling the propagation of wave packets, such as diffractionless self-splitting beams and collimated wave propagations. In addition, we show the two subsystems both undergo an identical topological phase transition, which allows us to explore Hermitian and non-Hermitian topological edge modes in a single system. As a potential application, we propose a coherent splitter that has locked phase and amplitudes at corresponding sites due to the decoupling between Hermitian and non-Hermitian subsystems. A recent study has demonstrated that a Dirac cone arises in a non-Hermitian system with both gain and loss which have pseudo-Hermiticity and anti-$\mathcal{PT}$ symmetries at the same time [67]. The major advantage of our approach is that DPs can be acquired in a passive platform without the necessity of any gain medium. We perform full wave simulation and show the proposed model can be realized in an evanescently coupled optical waveguide. The proposed mechanism is valid for other tight-binding systems and its extension to multiple chains and high- dimensional systems is also possible, which may develop alternative directions for exploring non-Hermitian physics.

ACKNOWLEDGMENTS

The work is supported by the Guangdong Major Project of Basic and Applied Basic Research (Grant No. 2019B030302003) and the National Natural Science Foundation of China (NSFC) (Grants No. 11804259 and No. 11974124).

[1] Y. Ota, K. Takata, T. Ozawa, A. Amo, Z. Jia, B. Kante, M. Notomi, Y. Arakawa, and S. Iwamoto, Active topological photonics, Nanophotonics **9**, 547 (2020).
[2] Z. Lin, L. Ding, S. Chen, S. Li, S. Ke, X. Li, and B. Wang, Photonic non-Bloch quadrupole topological insulators in coupled ring resonators, Phys. Rev. A **103**, 063507 (2021).
[3] Z. Lin, L. Ding, S. Ke, and X. Li, Steering non-Hermitian skin modes by synthetic gauge fields in optical ring resonators, Opt. Lett. **46**, 3512 (2021).
[4] Z. Lin, S. Ke, X. Zhu, and X. Li, Square-root non-Bloch topological insulators in non-Hermitian ring resonators, Opt. Express **29**, 8462 (2021).
[5] L. Ding, Z. Lin, S. Ke, B. Wang, and P. Lu, Non-Hermitian flat bands in rhombic microring resonator arrays, Opt. Express **29**, 24373 (2021).
[6] S. Ke, D. Zhao, J. Fu, Q. Liao, B. Wang, and P. Lu, Topological edge modes in non-hermitian photonic aharonov-bohm cages, IEEE J. Sel. Top. Quantum Electron. **26**, 4401008 (2020).
[7] E. J. Bergholtz, J. C. Budich, and F. K. Kunst, Exceptional topology of non-Hermitian systems, Rev. Mod. Phys. **93**, 015005 (2021).
[8] M. Golshani, S. Weimann, K. Jafari, M. K. Nezhad, A. Langari, A. R. Bahrampour, T. Eichelkraut, S. M. Mahdavi, and A. Szameit, Impact of Loss on the Wave Dynamics in Photonic Waveguide Lattices, Phys. Rev. Lett. **113**, 123903 (2014).
[9] C. Yuce and H. Ramezani, Topological states in a non-Hermitian two-dimensional Su-Schrieffer-Heeger model, Phys. Rev. A **100**, 032102 (2019).
[10] H. Guo and D. Zhao, Giant spatial Goos–Hänchen shifts in a non-Hermitian dielectric slab sandwiched by graphene, Optik **242**, 167332 (2021).
[11] M. C. Zheng, D. N. Christodoulides, R. Fleischmann, and T. Kottos, $\mathscr{PT}$ optical lattices and universality in beam dynamics, Phys. Rev. A **82**, 010103(R) (2010).
[12] R. El-Ganainy, K. G. Makris, M. Khajavikhan, Z. H. Musslimani, S. Rotter, and D. N. Christodoulides, Non-Hermitian physics and $\mathcal{PT}$ symmetry, Nat. Phys. **14**, 11 (2018).
[13] K. G. Makris, R. El-Ganainy, D. N. Christodoulides, and Z. H. Musslimani, Beam Dynamics in $\mathcal{PT}$ Symmetric Optical Lattices, Phys. Rev. Lett. **100**, 103904 (2008).
[14] S. Ke, D. Zhao, J. Liu, Q. Liu, Q. Liao, B. Wang, and P. Lu, Topological bound modes in anti-$\mathcal{PT}$-symmetric optical waveguide arrays, Opt. Express **27**, 13858 (2019).
[15] K. Kawabata and M. Sato, Real spectra in non-Hermitian topological insulators, Phys. Rev. Research **2**, 033391 (2020).

[16] H. H. Chun-Hui Liu and S. Chen, Symmetry and topological classification of Floquet non-Hermitian systems, arXiv:2112.06715.

[17] Y. Long, H. Xue, and B. Zhang, Real-eigenvalued non-Hermitian topological systems without parity-time symmetry, arXiv:2111.02701.

[18] N. P. Armitage, E. J. Mele, and A. Vishwanath, Weyl and Dirac semimetals in three-dimensional solids, Rev. Mod. Phys. **90**, 015001 (2018).

[19] S. H. Nam, A. J. Taylor, and A. Efimov, Diabolical point and conical-like diffraction in periodic plasmonic nanostructures, Opt. Express **18**, 10120 (2010).

[20] X. Liu, J. Yang, X. Guo, J. Zhang, P. Li, and Y. Liu, Conical diffractions in kagome lattice, Results Phys. **23**, 104007 (2021).

[21] K. S. Novoselov, A. K. Geim, S. V. Morozov, D. Jiang, M. I. Katsnelson, I. V. Grigorieva, S. V. Dubonos, and A. A. Firsov, Two-dimensional gas of massless Dirac fermions in graphene, Nature (London) **438**, 197 (2005).

[22] B. Xu, T. Li, and S. Zhu, Simulation of massless Dirac dynamics in plasmonic waveguide arrays, Opt. Express **26**, 13416 (2018).

[23] S. H. Nam, J. Zhou, A. J. Taylor, and A. Efimov, Dirac dynamics in one-dimensional graphene-like plasmonic crystals: Pseudo-spin, chirality, and diffraction anomaly, Opt. Express **18**, 25329 (2010).

[24] N. Zhang and S. C. Chen, Formation of nanostructures and optical analogues of massless Dirac particles via femtosecond lasers, Opt. Express **28**, 36109 (2020).

[25] J. M. Zeuner, N. K. Efremidis, R. Keil, F. Dreisow, D. N. Christodoulides, A. Tunnermann, S. Nolte, and A. Szameit, Optical Analogues for Massless Dirac Particles and Conical Diffraction in One Dimension, Phys. Rev. Lett. **109**, 023602 (2012).

[26] N. Fu, Z. Fu, H. Zhang, Q. Liao, D. Zhao, and S. Ke, Topological bound modes in optical waveguide arrays with alternating positive and negative couplings, Opt. Quantum Electron. **52**, 61 (2020).

[27] M. Milićević, G. Montambaux, T. Ozawa, O. Jamadi, B. Real, I. Sagnes, A. Lemaître, L. Le Gratiet, A. Harouri, J. Bloch, and A. Amo, Type-III and Tilted Dirac Cones Emerging from Flat Bands in Photonic Orbital Graphene, Phys. Rev. X **9**, 031010 (2019).

[28] C. Hu, Z. Li, R. Tong, X. Wu, Z. Xia, L. Wang, S. Li, Y. Huang, S. Wang, B. Hou, C. T. Chan, and W. Wen, Type-II Dirac Photons at Metasurfaces, Phys. Rev. Lett. **121**, 024301 (2018).

[29] C. T. Chan, Z. H. Hang, and X. Huang, Dirac dispersion in two-dimensional photonic crystals, Adv. OptoElectron. **2012**, 313984 (2012).

[30] L. Lu, J. D. Joannopoulos, and M. Soljačić, Topological photonics, Nat. Photonics **8**, 821 (2014).

[31] W. Zhang, X. Chen, and F. Ye, Plasmonic topological insulators for topological nanophotonics, Opt. Lett. **42**, 4063 (2017).

[32] Y.-X. Xiao, K. Ding, R.-Y. Zhang, Z. H. Hang, and C. T. Chan, Exceptional points make an astroid in non-Hermitian Lieb lattice: Evolution and topological protection, Phys. Rev. B **102**, 245144 (2020).

[33] H. C. Wu, X. M. Yang, L. Jin, and Z. Song, Untying links through anti-parity-time-symmetric coupling, Phys. Rev. B **102**, 161101(R) (2020).

[34] M. Dehghani, C. Yuce, T. Kottos, and H. Ramezani, Constant intensity conical diffraction in discrete one-dimensional lattices with charge-conjugation symmetry, Opt. Lett. **45**, 101 (2019).

[35] A. Tuniz, T. Wieduwilt, and M. A. Schmidt, Tuning the Effective $\mathcal{PT}$ Phase of Plasmonic Eigenmodes, Phys. Rev. Lett. **123**, 213903 (2019).

[36] H. Hodaei, A. U. Hassan, S. Wittek, H. Garcia-Gracia, R. El-Ganainy, D. N. Christodoulides, and M. Khajavikhan, Enhanced sensitivity at higher-order exceptional points, Nature (London) **548**, 187 (2017).

[37] Y.-R. Zhang, Z.-Z. Zhang, J.-Q. Yuan, M. Kang, and J. Chen, High-order exceptional points in non-Hermitian moiré lattices, Front. Phys. **14**, 53603 (2019).

[38] S. M. Zhang, X. Z. Zhang, L. Jin, and Z. Song, High-order exceptional points in supersymmetric arrays, Phys. Rev. A **101**, 033820 (2020).

[39] S. Liu, S. Ma, C. Yang, L. Zhang, W. Gao, Y. J. Xiang, T. J. Cui, and S. Zhang, Gain- and Loss-Induced Topological Insulating Phase in a Non-Hermitian Electrical Circuit, Phys. Rev. Appl. **13**, 014047 (2020).

[40] S. Yao and Z. Wang, Edge States and Topological Invariants of Non-Hermitian Systems, Phys. Rev. Lett. **121**, 086803 (2018).

[41] T. Liu, Y. R. Zhang, Q. Ai, Z. Gong, K. Kawabata, M. Ueda, and F. Nori, Second-Order Topological Phases in Non-Hermitian Systems, Phys. Rev. Lett. **122**, 076801 (2019).

[42] W. Song, W. Sun, C. Chen, Q. Song, S. Xiao, S. Zhu, and T. Li, Breakup and Recovery of Topological Zero Modes in Finite Non-Hermitian Optical Lattices, Phys. Rev. Lett. **123**, 165701 (2019).

[43] W. Zhu, X. Fang, D. Li, Y. Sun, Y. Li, Y. Jing, and H. Chen, Simultaneous Observation of a Topological Edge State and Exceptional Point in an Open and Non-Hermitian Acoustic System, Phys. Rev. Lett. **121**, 124501 (2018).

[44] J. Song, F. Yang, Z. Guo, X. Wu, K. Zhu, J. Jiang, Y. Sun, Y. Li, H. Jiang, and H. Chen, Wireless Power Transfer via Topological Modes in Dimer Chains, Phys. Rev. Appl. **15**, 014009 (2021).

[45] A. U. Hassan, B. Zhen, M. Soljacic, M. Khajavikhan, and D. N. Christodoulides, Dynamically Encircling Exceptional Points: Exact Evolution and Polarization State Conversion, Phys. Rev. Lett. **118**, 093002 (2017).

[46] Y. H. Lai, Y. K. Lu, M. G. Suh, Z. Yuan, and K. Vahala, Observation of the exceptional-point-enhanced Sagnac effect, Nature (London) **576**, 65 (2019).

[47] S. Weimann, M. Kremer, Y. Plotnik, Y. Lumer, S. Nolte, K. G. Makris, M. Segev, M. C. Rechtsman, and A. Szameit, Topologically protected bound states in photonic parity-time-symmetric crystals, Nat. Mater. **16**, 433 (2017).

[48] B. Zhen, C. W. Hsu, Y. Igarashi, L. Lu, I. Kaminer, A. Pick, S. L. Chua, J. D. Joannopoulos, and M. Soljacic, Spawning rings of exceptional points out of Dirac cones, Nature (London) **525**, 354 (2015).

[49] M. Kang, W. Zhu, H. T. Wang, and M. Premaratne, Spawning a ring of exceptional points from a metamaterial, Opt. Express **25**, 18265 (2017).

[50] A. Cerjan, S. Huang, M. Wang, K. P. Chen, Y. Chong, and M. C. Rechtsman, Experimental realization of a Weyl exceptional ring, Nat. Photonics **13**, 623 (2019).

[51] X. F. Zhu, Defect states and exceptional point splitting in the band gaps of one-dimensional parity-time lattices, Opt. Express **23**, 22274 (2015).

[52] L. Tang, D. Song, S. Xia, S. Xia, J. Ma, W. Yan, Y. Hu, J. Xu, D. Leykam, and Z. Chen, Photonic flat-band lattices and unconventional light localization, Nanophotonics **9**, 1161 (2020).

[53] S. Mukherjee, A. Spracklen, D. Choudhury, N. Goldman, P. Ohberg, E. Andersson, and R. R. Thomson, Observation of a Localized Flat-Band State in a Photonic Lieb Lattice, Phys. Rev. Lett. **114**, 245504 (2015).

[54] S. Flannigan, L. Madail, R. G. Dias, and A. Daley, Hubbard models and state preparation in an optical Lieb lattice, New J. Phys. **23**, 083014 (2021).

[55] W. X. Teo, L. Li, X. Zhang, and J. Gong, Topological characterization of non-Hermitian multiband systems using Majorana's stellar representation, Phys. Rev. B **101**, 205309 (2020).

[56] J. Bartlett, H. Hu, and E. Zhao, Illuminating the bulk-boundary correspondence of a non-Hermitian stub lattice with Majorana stars, Phys. Rev. B **104**, 195131 (2021).

[57] Y. X. Xiao, G. Ma, Z. Q. Zhang, and C. T. Chan, Topological Subspace-Induced Bound State in the Continuum, Phys. Rev. Lett. **118**, 166803 (2017).

[58] G. Pelegrí, A. M. Marques, R. G. Dias, A. J. Daley, V. Ahufinger, and J. Mompart, Topological edge states with ultracold atoms carrying orbital angular momentum in a diamond chain, Phys. Rev. A **99**, 023612 (2019).

[59] T. Mizoguchi, Y. Kuno, and Y. Hatsugai, Square-root higher-order topological insulator on a decorated honeycomb lattice, Phys. Rev. A **102**, 033527 (2020).

[60] M. Kremer, I. Petrides, E. Meyer, M. Heinrich, O. Zilberberg, and A. Szameit, A square-root topological insulator with non-quantized indices realized with photonic Aharonov-Bohm cages, Nat. Commun. **11**, 907 (2020).

[61] M. Ezawa, Systematic construction of square-root topological insulators and superconductors, Phys. Rev. Research **2**, 033397 (2020).

[62] A. M. Marques, L. Madail, and R. G. Dias, One-dimensional 2n-root topological insulators and superconductors, Phys. Rev. B **103**, 235425 (2021).

[63] Y. X. Xiao, Z. Q. Zhang, and C. T. Chan, A band of bound states in the continuum induced by disorder, Sci. Rep. **8**, 5160 (2018).

[64] P. Delplace, T. Yoshida, and Y. Hatsugai, Symmetry-Protected Multifold Exceptional Points and Their Topological Characterization, Phys. Rev. Lett. **127**, 186602 (2021).

[65] B. Wang, X. Zhang, F. J. Garcia-Vidal, X. Yuan, and J. Teng, Strong Coupling of Surface Plasmon Polaritons in Monolayer Graphene Sheet Arrays, Phys. Rev. Lett. **109**, 073901 (2012).

[66] A. Szameit, T. Pertsch, F. Dreisow, S. Nolte, A. Tünnermann, U. Peschel, and F. Lederer, Light evolution in arbitrary two-dimensional waveguide arrays, Phys. Rev. A **75**, 053814 (2007).

[67] H. Xue, Q. Wang, B. Zhang, and Y. D. Chong, Non-Hermitian Dirac Cones, Phys. Rev. Lett. **124**, 236403 (2020).